Research paper

Numerical and experimental analysis of powder bed homogeneity through multi-layer spreading in additive manufacturing

Sujith Reddy Jaggannagari [a], Wen Hao Kan [b], Louis N.S. Chiu [d], Gwénaëlle Proust [b,c], Aijun Huang [d], Yixiang Gan [c], Ratna Kumar Annabattula [a,e,*]

[a] Mechanics of Materials Laboratory, Department of Mechanical Engineering, Indian Institute of Technology Madras, Chennai 600036, India
[b] Sydney Manufacturing Hub, The University of Sydney, NSW 2006, Australia
[c] School of Civil Engineering, The University of Sydney, NSW 2006, Australia
[d] Department of Materials Science and Engineering, Monash University, Clayton, VIC, Australia
[e] Additive Manufacturing Group - Centre of Excellence in Materials and Manufacturing for Futuristic Mobility, Indian Institute of Technology Madras, Chennai 600036, India

ARTICLE INFO

ABSTRACT

The generation of a uniform and homogeneous powder bed under various process parameters is essential for ensuring high-quality final products in laser powder bed fusion (LPBF) additive manufacturing. In this work, powder bed homogeneity is analysed using experiments and discrete element method (DEM) simulations. The experimental investigations revealed variation in the particle size distributions in the extreme zones of the spreading platform, indicating segregation within the powder bed. Scaled DEM simulations were carried out to analyse the multi-layer spreading process with a fully modelled dispenser. The results showed that the packing density of the spread layer initially increases during the spreading process and then reaches a constant value of approximately 56%, which is in good agreement with the experimental findings. The simulation results also revealed the variation in the packing density and particle size distribution in different zones of the spreading platform. This study provides detailed analyses of the influence of process parameters such as dosing factor, first layer thickness and recoater velocity on the powder bed homogeneity. Higher dosing factors and increased first layer thickness improve packing density but do not eliminate segregation effects, whereas higher recoater velocities decrease packing density and surface quality while reducing segregation. The findings contribute to a better understanding of the powder spreading mechanism in LPBF and provide insights to improve the overall bed quality.

1. Introduction

Laser powder bed fusion (LPBF) is an additive manufacturing technique that involves the spreading of thin layers of metal powder, followed by selective fusion using a laser [1,2]. This process is repeated in a layer-by-layer manner until the desired shape and size are achieved. Compared to conventional manufacturing techniques, LPBF provides the capability for near-net shape manufacturing of intricate geometries [1,3]. LPBF involves complex and numerous process parameters in the spreading and melting processes. Extensive research has been carried out to understand the influence of process parameters on the quality of the powder bed and the manufactured parts [3–9]. This study aims to analyse and optimise the process parameters specific to the powder spreading process.

The powder spreading is a fundamental and crucial process of LPBF, and the quality of the powder bed plays a key role in determining the porosity and strength and, hence, the structural and mechanical properties of the manufactured parts [10–13]. The generation of uniform and homogeneous powder bed is a complex phenomenon influenced by powder characteristics and process parameters. Over the past decade, extensive experiments [6,14–17] and discrete element method (DEM) simulations [4,18–21] have been conducted to understand the underlying mechanisms, thereby optimising powder characteristics and process parameters. To form thin, dense, and uniform layers, powders must exhibit suitable rheological properties. In this context, the terms 'flowability' and 'spreadability' are employed to characterise the capabilities of powders to flow and spread, respectively [19,22]. Flowability refers to the degree to which a particle moves in relation

---

to neighbouring particles or along the recoater surface, significantly impacting the detachment of particles from piles and the replenishment of depleted regions within those piles [22]. The flowability of a powder is significantly affected by a range of factors such as particle shape and size distribution, chemical composition, moisture content, particle stiffness, density, electrostatic charge, and porosity [23–27]. Conversely, spreadability refers to the powder's ability to be uniformly distributed as a thin layer, free from voids and agglomerates [19]. The spreadability of powders is governed by spreader speed and geometry, layer thickness, dosing factor, spreader material type, and temperature and moisture content of powder [16,24,28–31]. Although flowability remains a fundamental property that significantly influences the ability of a powder to form thin, dense, and uniform layers, this study focuses on the spreadability of the powder, emphasising its critical importance in the context of powder bed additive manufacturing.

Ahmed et al. [32] introduced an experimental technique to assess the spreadability of powder in additive manufacturing, focusing on the impact of blade gap height on the uniformity of spread layers, demonstrated through the analysis of empty patches and jamming phenomena. Nan and Gu [22] examined the spreadability of cohesive and friction powder experimentally. The authors explored the impact of operational conditions and particle characteristics on the spreadability of metal powders essential for additive manufacturing. Findings highlight that spreadability varies non-linearly with spreading speed, and optimal conditions exist for achieving superior layer uniformity. It differentiates between spreadability and flowability, suggesting targeted adjustments in powder properties can optimise final printed parts. Chen et al. [33] conducted experiments to examine the relationship between the surface roughness of Ti64 alloy components and their positioning on the build platform. Additionally, the authors observed that the variation in surface roughness is attributed to the varying powder size distribution across the platform. Extracting precise dynamic data of the powder bed quality from the experiments poses a major challenge to acquiring detailed information at the particle level to understand the mechanisms influenced by process parameters. The limitations of the physical experiments can be overcome through computer simulations. Discrete element modelling (DEM) is a method widely adopted by researchers to replicate and address the limitations encountered in experiments. DEM was originally proposed by Cundall and Strack [34], and it is based on Newton's law of motion and can describe the dynamic behaviour of powder. Chen et al. [35] examined variations in particle size that affect the packing density and homogeneity of the powder bed. Their study found that increasing particle size when the particle size range $D \geq 30\,\mu\text{m}$ or decreasing particle size when $D < 30\,\mu\text{m}$ results in reduced packing density and homogeneity of the powder bed. Additionally, authors investigated the distinct mechanical behaviours exhibited by large and small particles. Large particles experience greater and more intense forces compared to their smaller particles. Consequently, this discrepancy in forces results in variations in velocities and motion behaviour between large and small particles, ultimately leading to segregation within the powder bed [36].

Layer thickness is defined as the distance by which the spreading platform is lowered for each layer, and this parameter highly influences the powder bed quality [35]. Mindt et al. [37] showed that when the layer thickness is less than the maximum powder particle size, it leads to lower packing density. An increase in the layer thickness increases the packing density and decreases the homogeneity of the powder bed. The force arch formed due to the lower layer gap hinders particle flow and hence decreases the quality of the powder layer. Additional decreases in the layer thickness increase the stress and voids in the deposited powder layer as reported by Chen et al. [35], Nan et al. [38].

The quality of the powder bed in LPBF is significantly influenced by the recoater material, geometry, and speed. The recoater material, typically a smooth or hard blade, plays a crucial role in evenly distributing the powder across the build platform [29,39–41]. The geometry of the recoater, including its angle and curvature, affects the powder flow and compaction, which in turn impacts the bed's uniformity and density [28,42]. Wang et al. [43] demonstrated that the recoater with inclined or round surfaces increases the efficiency of powder spreading. Furthermore, the recoater speed, which controls the rate at which the powder is spread, influences the packing density and the formation of defects such as powder piles and voids [44].

As mentioned above, extensive research has focused on the impact of various process parameters, including particle size and shape distribution, layer thickness, and recoater speed, on the quality of the powder bed, as listed in Table 1. However, the influence of the dosing factor has received comparatively little attention in previous studies, with only a few experimental investigations addressing it [30,31,45, 46]. The dosing factor measures the quantity of powder deposited from the dispenser onto the spreading platform in each layer of the LPBF process [45]. In other words, the dosing factor for the specific layer is the ratio of the volume of the metal powder used to the theoretical volume of the spread zone [30]. To understand the effect of the dosing factor on powder bed quality, it is essential to analyse the process of multi-layer powder spreading. Previous studies on multi-layer powder spreading typically simulated the process without explicitly incorporating a powder dispenser [47–50]. In those cases, powders were deposited as a particle cloud, which then settled under gravity in front of the recoater for spreading. In contrast, our work includes a fully modelled powder dispenser as part of the spreading simulation. This approach is crucial because it replicates the realistic additive manufacturing process more accurately, capturing the cumulative impact of dosing over successive layers. This involves conducting computationally extensive simulations in order to investigate thoroughly.

The aim of this study is thus to develop a discrete element modelling framework for spreading cohesive powders, integrating the scaling and computing techniques such as a dynamic domain with a graphics processing unit (GPU) solver to minimise the computational cost of multi-layer spreading with the fully modelled dispenser. The quality of the powder bed layer is quantitatively evaluated using packing density and particle size distribution (PSD) and compared with the experimental findings. Investigated the influence of the process parameters such as dosing factor, first layer thickness and recoater velocity on the homogeneity of the powder bed. To the best of our knowledge, the effect of the dosing factor and first-layer thickness has not been extensively explored in the literature through multi-layer spreading simulations. These findings significantly enhance the understanding of the mechanism of powder spreading on pre-existing layers on the platform.

2. Methodology

2.1. Experimental investigation

The experiments were conducted to analyse the particle size distribution of the powder in extreme zones of the spreading platform. In these experiments, an EOS M290 printer with the platform dimensions of 250 mm × 250 mm is used. The direction of the spreading and the gas flow is shown in Fig. 1(a), and a flat silicone recoater moves with a constant velocity of 150 mm s^{-1} to spread the powder onto the platform. The recoater thickness was measured to be a 7 mm parallel to the powder surface. The corner angle was approximately 74°, indicating a slight taper. The powder used in this study is a commercially available spherical powder supplied by AP&C, specifically designed and optimised for laser powder bed fusion (LPBF) processes. The variation in the particle size distribution of powder in different zones of the build platform is investigated experimentally by printing boxes to collect the powder samples (see Fig. 1(a)). The boxes are printed at the extreme ends of the platform and are named as beginning zone and end zone, respectively, as shown in Fig. 1(a). The square boxes have internal dimensions of 30 mm in side length (L_B), 3 mm in wall thickness (T_B), and 16 mm in height (H_B) (see Fig. 1(a)). Each box also has a

Table 1
List of powders, particle sizes, surface energy and recoater velocities used in previous studies.

References	Powders	Size range(μm)	$D_{10}/D_{50}/D_{90}$ (μm)	Surface energy (mJ m^{-2})	Layer thickness (μm)	Recoater velocity (mm s^{-1})
Nan et al. [38] (Exp and Sim)	316L stainless steel	15–55	20/32/45	1.4	67.5, 90, 112.5, 135	80
Xiang et al. [51] (Exp and Sim)	316L stainless steel	15–53	$D_{mean} = 30$	0.1	60, 80, 100, 150, 200	50
Si et al. [52] (Sim)	PA6	9.86–86.4	$D_{50} = 41.1$	0.013	82.2, 123.3, 164.4, 205.5	50
Yao et al. [53] (Sim)	316L stainless steel	–	$D_{50} = 65$	1	65, 130, 162.5, 195	100
Stephan et al. [18] (Sim)	316L stainless steel	4.7–54.7	10/18/32	0–1	60	50
Wu et al. [4] (Exp and Sim)	Molybdenum (Mo)	15–78	26/36/50	0.06	77.5, 100, 1.25, 150, 175	25, 50, 80, 100, 150
Wu et al. [54] (Exp and Sim)	2195 Al alloy	2.2–90	24.18/40.27/59.82	0.2, 0.5, 0.8, 1.1	30, 60, 93, 120	–
Mussatto et al. [24] (Exp)	316L Stainless steel	15–78	15.6/31.8/55.5 25.7/36.7/61.6 18.3/28/42.4	–	30, 50, 70	10, 80, 160
Xu and Nan [19] (Sim)	316L stainless steel	15–55	20/32/45	1.4, 5.2, 9, 11.2	50, 100, 150	80

Note: Sim denotes Simulations, Exp denotes Experiments.

printed base of 2 mm in height, and the collected powder was spread between a height of 2 mm to 18 mm to ensure that powder spreading has stabilised before the PSD analysis. For this experiment, a dosing factor of one and layer thickness of 30 μm were used. After the process, powder samples were scooped up manually from each of the printed boxes, and the empty boxes after scooping are shown in Fig. 1(b). The collected powder was analysed using a laser diffraction test using HELOS (H3751) and RODOS/T4, the R4 series of Sympatec GmbH machines, and the software used was PAQXOS 2.2.2. The powder samples collected from each box, as well as the original powder used for printing, were tested twice. The particle size distribution of the powder used for spreading (original powder) is shown in Fig. 1(c). The PSD in the experiments is based on volume, which may undercount the number of fine particles in the distribution. The variation of the particle size distribution in different zones of the platform is presented in Section 3.1. Additionally, at every layer, the walls of the square boxes are printed, as shown in red colour in Fig. 1(d). Hence, the print volume is relatively small compared to the total powder volume spread on the build platform. As the print volume is low, the melting effects were not accounted for in the simulations. Furthermore, after each printing step, the platform is lowered for the subsequent spreading process (see Fig. 1(d)). Consequently, the particles do not encounter the wall in the direction of spreading; only the bottom-most particles get deposited on the solidified surface of the walls. The simulation setup is explained in the subsequent section.

2.2. Simulation setup and DEM modelling

The multi-layer spreading setup consists of a dispenser and spreading platforms with respective lengths of L_D, L_S and width (W), as shown in Fig. 2(a). The metal powder, characterised by its particle size distribution (PSD) with volume-based D_{10}, D_{50}, and D_{90} of 22.66 μm, 36.52 μm, and 54.03 μm respectively, is filled in the dispenser. The PSD of powder in simulations is exactly similar to the powder used in the experiments, as shown in Fig. 1(c). The quantity of powder generated in the dispenser is sufficient to spread about 16 layers, with a dosing factor of one. The sequence of steps for the spreading process is as follows: (i) Rising of the dispenser platform based on the dosing factor (D_F) by $H_D = D_F \frac{H \times A_S}{A_D}$, where H is the layer thickness, A_S and A_D are the areas of the spreading and dispenser platforms respectively (see Fig. 2(b)). (ii) Lowering the spreading platform based on the

layer thickness (H). (iii) Forward motion of the recoater for powder spreading with a constant velocity (V_R) along the X-direction until the end of the spreading platform. (iv) Returning the recoater to the initial position with a constant velocity. This sequence of steps is shown in Fig. 2(b), and it repeats for several layers similar to the experiments. For the simulations, a flat recoater with a thickness of 0.125 mm was used, featuring a corner angle of 90° and no corner radius. This choice of recoater dimensions and geometry was made to account for the reduced length of the simulation domain and to simplify the simulation complexity, consistent with previous studies [18,19]. The periodic boundary condition is used along the width of the setup (Y-direction), and the gravitational force is along the negative Z-direction. The values of the parameters used in the simulation are listed in Table 2.

The analysis of inter-particle interactions during all the processes mentioned above is carried out using DEM. Johnson–Kendall–Roberts (JKR) with Hertz-Mindlin (HM) contact model incorporating the van der Waals force of attraction is used to describe the cohesive interactions among powder particles. The normal contact force ($F_{ij}^{n,c}$) in the JKR model and the relationship between the contact radius (r_c), the normal overlap (δ_{ij}^n) and cutoff overlap (δ_{cutoff}^n) are given in Eqs. (2.1)–(2.3) respectively.

$$F_{ij}^{n,c} = \frac{4E^*}{3R^*}r_c^3\hat{n} - \sqrt{8\pi E^*\Gamma}\ r_c^{\frac{3}{2}}\hat{n} \tag{2.1}$$

$$r_c^4 - 2\delta_{ij}^n R^*\ r_c^2 - \frac{2\pi\Gamma R^{*2}}{E^*}r_c + \delta_{ij}^{n\,2}R^{*2} = 0 \tag{2.2}$$

$$\delta_{cutoff}^n = -\left(\frac{3(F_{ij}^n)_{pullout}^2}{16R^*E^{*2}}\right)^{\frac{1}{3}} \tag{2.3}$$

where E^* and R^* are the effective Young's modulus and effective particle radius, respectively. The cohesive interaction is governed by the work of adhesion or interfacial surface energy (Γ), and the maximum cohesive force, also called the pullout force, is given by $(F_{ij}^n)_{pullout} = \frac{3}{2}\pi R^*\Gamma$. Further details of the contact model and other equations used for the DEM framework are briefly described in the supplementary material.

The computational cost is very high to simulate the spreading process of metal powders due to their micron size and high Young's modulus. The DEM timestep, based on the Rayleigh critical time, is given by $\left(t_c = \frac{\pi R \sqrt{\frac{\rho \times 2(1+\nu)}{E}}}{0.1631\nu + 0.8766}\right)$. Thereby, an increase in the particle

(a)

(b)

(c)

(d)
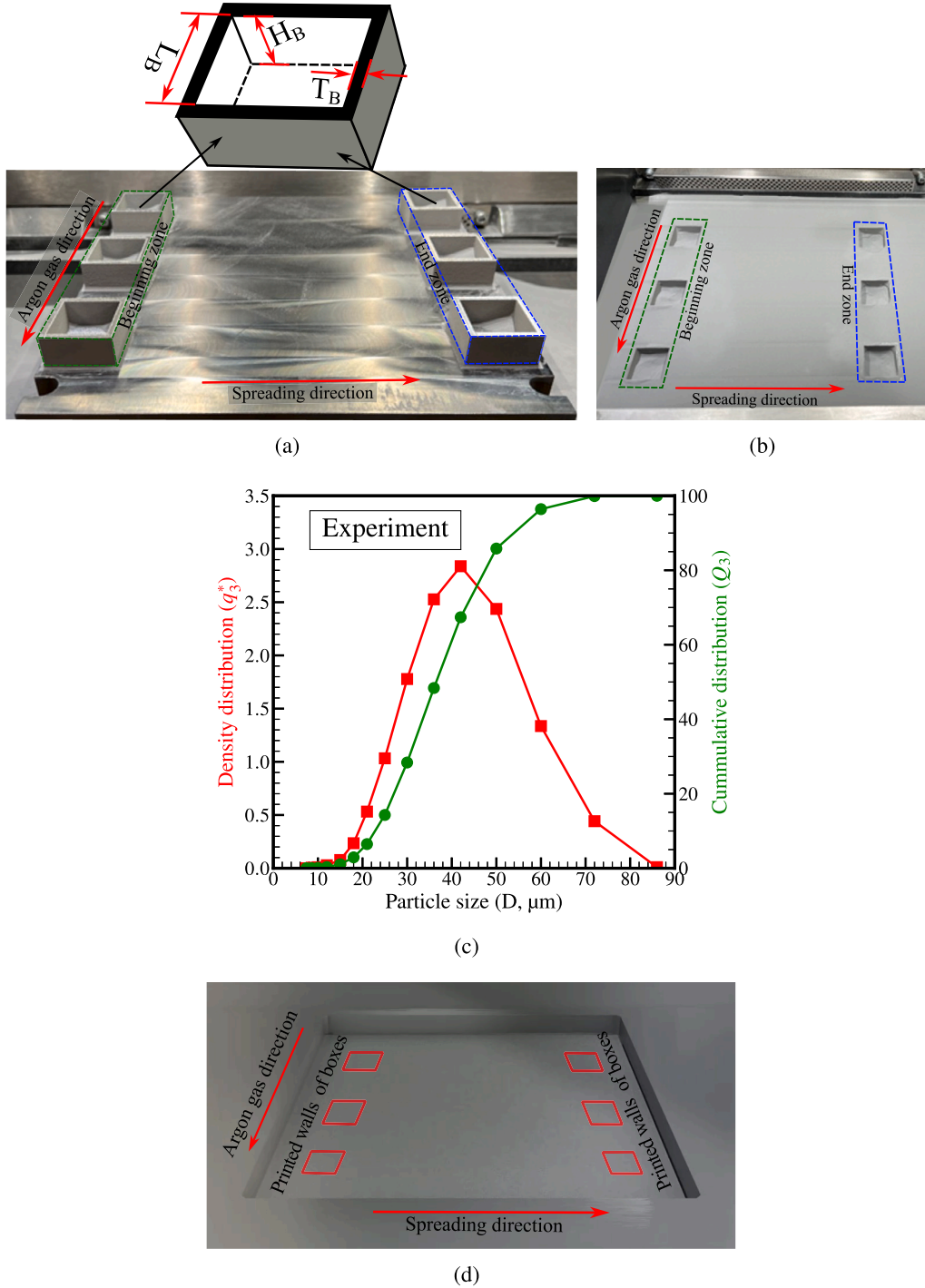
Fig. 1. (a) Arrangement of square boxes for collection of powder during spreading, (b) platform illustrating the square boxes after collection of the powders, (c) particle size distribution of original powder used for spreading, and (d) illustration of the printed box in the experiments. The printed walls of the boxes are indicated in red colour, and the build platform is lowered for the subsequent spreading process.

size or density and a decrease in Young's modulus reduce the cost of computation. In this work, the particle size and density are considered exactly as the experimental values. The reduction of the computational cost is done in two folds to carry out multi-layer spreading simulation: (i) Implementation of a scaling law to alter Young's modulus and cohesion parameter, and (ii) use of dynamic domain feature and GPU solver. Considering a reduced value of Young's modulus leads to a higher time-step and thereby lowers the computational cost. As the cohesive contact model is used, if the cohesion parameter (Γ) is not scaled down appropriately, it would result in a more cohesive collision

as the kinetic energy lost upon collision increases significantly. The modification of Young's modulus (E), as well as the surface energy (Γ), should also ensure that the cohesion number is not changed. The cohesion number [55] is the ratio of work of cohesion over the particle gravitational potential energy (see Eq. (2.4)).

$$\text{Cohesion number} = \frac{1}{\rho g}\left[\frac{\Gamma^5}{E^{*2}R^{*8}}\right]^{1/3} \tag{2.4}$$

Further, modified surface energy (Γ_{mod}) in terms of modified Young's modulus (E_{mod}) can be expressed as Eq. (2.5) [56]. It can be noticed
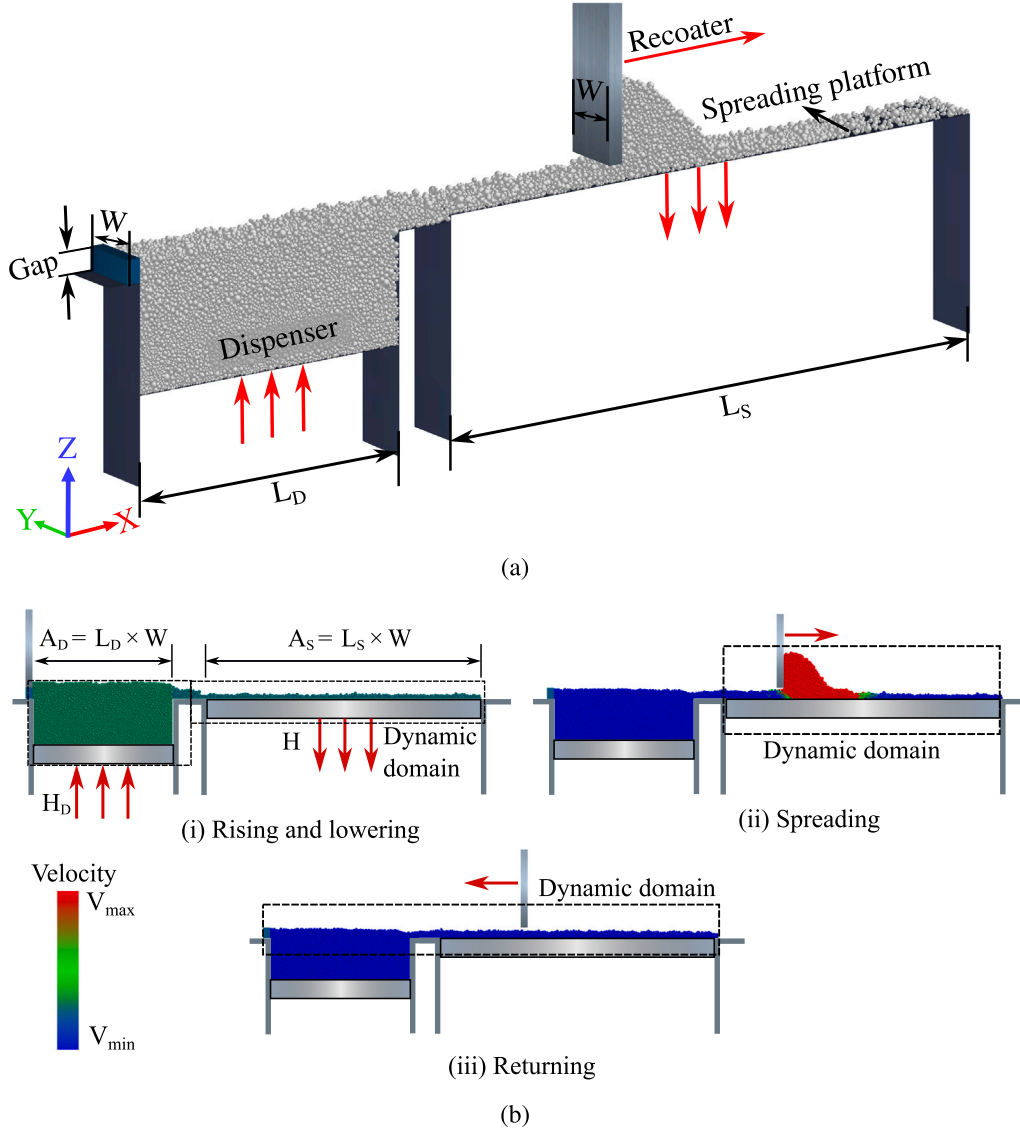
Fig. 2. (a) Schematic diagram of multi-layer powder spreading setup, and (b) visualisation of the sequence of steps.

Table 2
Values of parameters used in the simulation.

Parameters	Value
Length of the dispenser (L_D)	$50D_{90}$
Length of the spreading platform (L_S)	$100D_{90}$
Width of the setup (W)	$10D_{90}$
Layer thickness (H, μm)	50
Dosing factor (D_F)	1
Recoater velocity (forward) (V_R, mm s^{-1})	50
Recoater velocity (return) (mm s^{-1})	200

that modification of Γ alters all the equations from Eqs. (2.1) to (2.3).

$$\Gamma_{\text{mod}} = \Gamma \left(\frac{E_{\text{mod}}}{E} \right)^{2/5} \qquad (2.5)$$

The selection of E and Γ for validation of the numerical model is presented in Section 2.3. The simulations are carried out in EDEM [57], an Altair DEM tool, and the dynamic domain feature and GPU solver are available in this tool. Using the dynamic domain feature, the particles that are not in action can be frozen, thereby not included in the DEM calculations. For instance, during the spreading process, only particles in front of the recoater and on the spreading platform (particles in the dashed box as shown in Fig. 2(b)) are actively considered for DEM computations. Particles outside this domain can be excluded from DEM calculations using the dynamic domain feature. Hence, the computation cost can be significantly reduced by enabling the scaling technique, the dynamic domain feature and GPU computation.

2.3. Model validation

In this section, the methodology for selecting suitable simulation parameters to validate the dynamic repose angle (DRA) of the powder pile is discussed. The DRA is one of the most widely used characterisation techniques to calibrate the accuracy of simulations against experimental data [35,53,54]. It is a critical indicator of powder flowability, which directly influences the spreadability of the powder [22]. In past studies, Young's modulus is reduced to a value 100 times lower than the experimental value [19,58]. In this current work, Young's modulus is reduced 10^4 times, and the surface energy (Γ) is modified based on the cohesion scaling law as mentioned in Section 2.2. In addition to E and Γ, other parameters such as coefficient of restitution, static friction, rolling friction, and recoater velocity need to be tuned to calibrate to match with experimental DRA. The selection of material properties, like the coefficient of restitution and the static friction coefficient, is
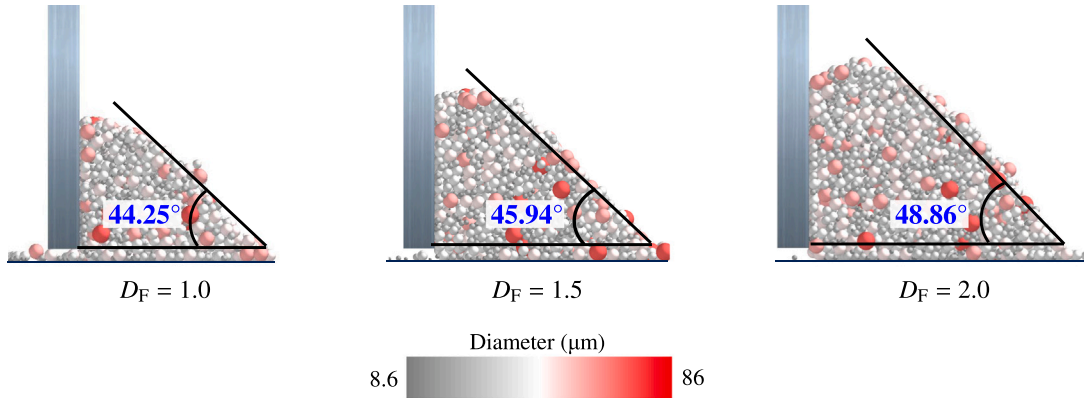
Fig. 3. Dynamic repose angle of the powder pile during spreading for different dosing factors.

Table 3
Material properties in the simulation.

Material properties	Particle	Geometry
Young's modulus (E, GPa)	210	–
Modified Young's modulus (E_{mod}, GPa)	0.021	0.021
Poisson's ratio (ν)	0.3	0.3
Density (ρ, kg m^{-3})	7980	7980
Surface energy (Γ, mJ m^{-2})	9	–
Modified surface energy (Γ_{mod}, mJ m^{-2})	0.2	–

Interaction parameters	Particle-Particle	Particle-Geometry
Coefficient of restitution (e)	0.64	0.64
Coefficient of static friction (μ_s)	0.5	0.5
Coefficient of rolling friction (μ_r)	0.1–0.2	0.1

based on the literature [19,38,58]. The rolling friction coefficient was determined iteratively by using different values in the simulations and aiming to obtain a repose angle of approximately 45°; the values fall within the range reported in the literature [18,35]. It was observed that the variation in the rolling friction coefficient within this range did not significantly influence the DRA, as also demonstrated by Shaheen et al. [5]. Additionally, the influence of recoater velocity on the DRA was investigated. Previous studies have demonstrated that the increase in the recoater velocity was found to increase the DRA [47,59]. To explore this effect further, a range of recoater velocities from 50 mm s^{-1} to 150 mm s^{-1} was analysed. It was found that the desired repose angle of approximately 45° could be achieved using a recoater velocity of 50 mm s^{-1}, while higher velocities resulted in greater variation and increased DRA. However, it may be noted that the fine-tuning of these parameters is done by trial and error rather than using an experimental technique, as in Khajepor et al. [60]. The material properties and interaction parameters considered for the simulations are provided in Table 3. The simulation parameters are within the range of values used in the literature (see Table 1). The determination of DRA was conducted as follows: as mentioned in Section 2.2, the powder spreading process is carried out with different dosing factors, and the DRA is estimated when the recoater is about half the length of the spreading platform. Fig. 3 shows that the DRA values for the powder are about 44.25°, 45.94°, and 48.86° with the dosing factors of 1, 1.5, 2, respectively. The DRA values are in good agreement with the experiments and simulation studies in the literature [53,54,61]. Furthermore, the packing density and particle size distribution of the spread layers, as detailed in subsequent sections, indicate the fidelity of the simulation model with respect to the experimental data.

3. Results and discussion

3.1. Multi-layer powder spreading simulation

As mentioned in Section 2.2, multiple layers of powder are spread onto the spreading platform. In particular, the simulation of powder

spreading of 16 layers with a dosing factor of one is presented in detail (see Movie C1). The evolution of the few spread layers is shown in Fig. 4(a). The powder dosing covers the entire length of the spreading platform for the first three layers. However, beyond the four layers, the powder dosing becomes insufficient to cover the entire length of the spreading platform, resulting in a wedge formation of the powder layer. The length of the wedge is represented as L_{wedge} (see Fig. 4(a)), and the reduction in the value of L_{wedge} as the spreading advances is correlated with packing density. The packing density (ϕ) is an important metric to describe the powder bed homogeneity. The packing density of the spread layer is estimated for two different volumes, i.e., whole volume and bulk volume, as shown in Fig. 4(b). The whole volume considers about 90% of the spreading platform length, with particles near the extreme ends (approximately length of $5 \times D_{50}$ from the ends [62,63]) excluded to avoid wall effects (grey-coloured particles as shown in Fig. 4(b)). In contrast, the bulk volume encompasses about 72% of the length (L_S), excluding particles in the wedge region and the topmost layer. The packing density for the whole and bulk volume is estimated as follows.

$$\text{Packing density } (\phi) = \frac{\sum V_{\text{par}}}{L \times W \times Z_H}, \tag{3.1}$$

where $\sum V_{\text{par}}$ is the total volume of the particles in whole or bulk volume, and L is the corresponding length of the volume ($L_W = 0.9 L_S$ and $L_B = 0.72 L_S$ for whole and bulk volume, respectively), Z_H is the corresponding height of the powder bed based on the volume (for whole volume $Z_H = Z_{\text{max}}$ and for bulk volume $Z_H = Z_{\text{max}} - D_{50}$), where Z_{max} is the maximum value of the z-coordinate among all the particles in the volume and L_S and W are provided in Table 2.

Fig. 4(c) illustrates the variation of packing density with the number of powder spread layers. The packing density for both the whole and bulk volumes increases with the number of layers and stabilises after a few layers (specifically, 12 layers for whole volume and 8 layers for bulk volume). The packing density of the whole volume stabilises at approximately 56%, a value consistent with experimental observations [33,64]. The reason for the low packing density for the initial few layers can be attributed to the wall effects of the spreading platform and the recoater and also the force arch formation leading to a phenomenon called jamming, as reported in several past studies [10,38, 53,54] (details are provided in supplementary material). Additionally, the spreading platform is assumed to be smooth and flat in simulations. However, achieving such ideal conditions in the experiments may not be feasible, leading to the first layer exhibiting poor quality. As the spreading process advances, these effects diminish due to an increase in the gap between the spreading platform and recoater, leading to enhanced powder deposition and increased packing density in subsequent layers. The porosity of the powder layer is initially high for the first few layers, and during spreading for subsequent layers, the powder dosing needs to compensate for the porosity of the previous layer (the localised
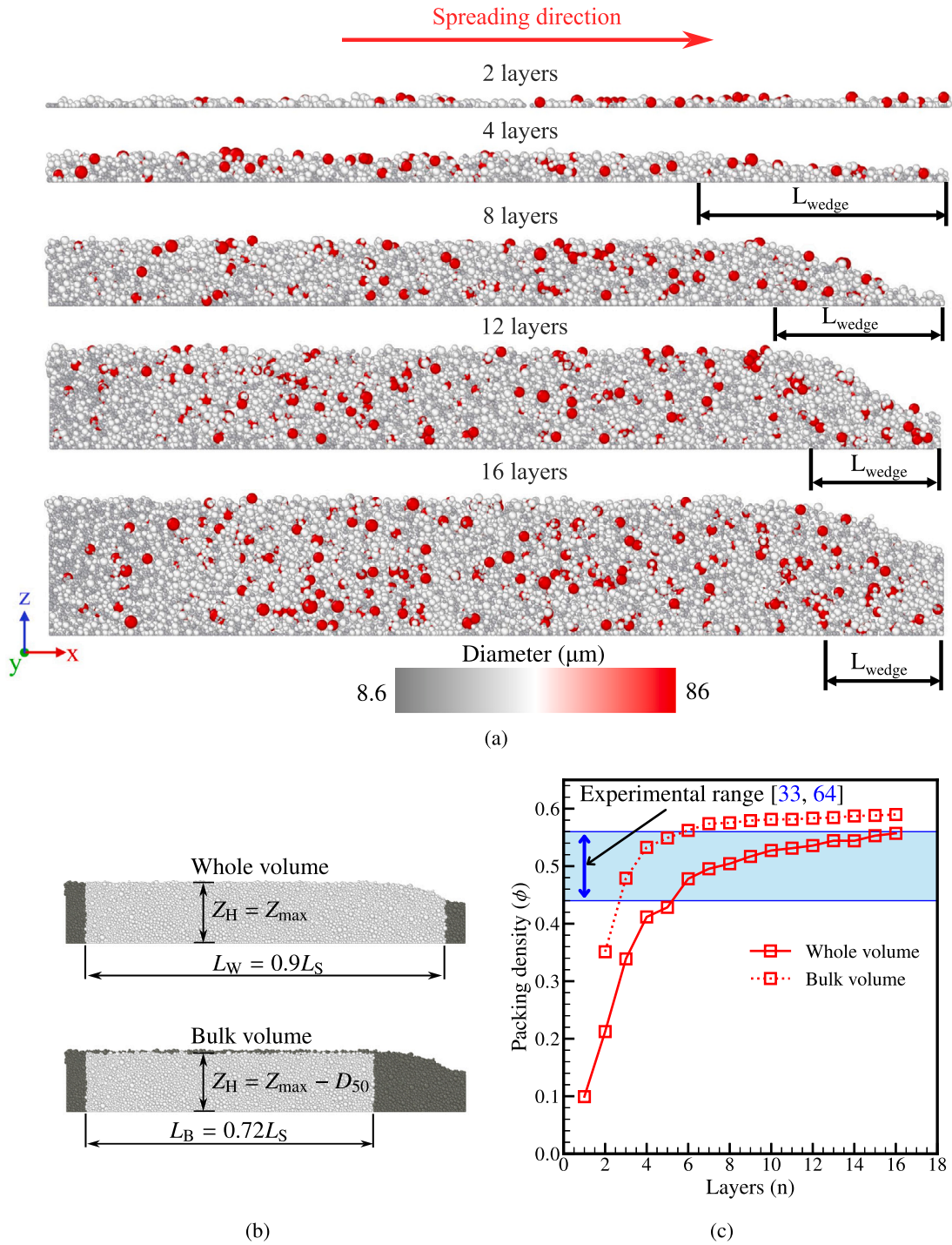
Fig. 4. Visualisation of the (a) spread layers, (b) bulk and whole volume for estimation of packing density, and (c) variation of packing density with the number of spread layers.

variation of the packing density of the sixteen layers is presented in the supplementary, indicating an increase in packing density in the bottom layers during spreading). This is not possible with the dosing factor of one, and hence, the powder will be insufficient at the end of the spreading platform. Furthermore, it can also be observed that once the packing density for the bulk volume is stabilised (8 layers in this case), the powder availability at the end of the spreading platform increases, which decreases the length of the wedge. Continuing the spreading process may eventually eliminate the wedge formation, after approximately 20 layers.

The powder bed with sixteen layers are further analysed to determine packing density and particle size distribution in different zones.

The powder bed is segmented into three equal zones, the Beginning (zone B), Centre zone (zone C), and End zone (zone E), indicated with respect to the particles' position on the spreading platform, as shown in Fig. 5(a), similar to the experiments detailed in Section 2.1. Considering the whole volume, the packing densities of zones B, C, and E are 0.5681, 0.5801, and 0.5136, respectively. Whereas for the bulk volume, the packing densities of zones B and E are almost similar, approximately 0.588, whereas the packing density of zone C (approximately 0.59) is slightly higher than that of zones B and E (see Fig. 5(a)). The experimental investigation demonstrated that the packing densities across all three zones are nearly identical [33], and the minimal differences observed in simulations between the centre and other zones indicate

Table 4

Comparison of D_{10}, D_{50}, and D_{90} values of PSD data from experimental and simulations.

Case	Zone	D_{10}	D_{50}	D_{90}
Experiment	Original	22.80	36.51	53.93
	Zone B	21.91	34.90	51.60
	Zone E	23.94	37.67	54.55
Simulation (Whole volume)	Original	22.66	36.52	54.03
	Zone B	21.72	34.45	51.30
	Zone E	24.00	38.31	55.61
Simulation (Bulk volume)	Zone B	21.70	34.44	51.38
	Zone E	23.39	37.40	55.06

Table 5

List of cases to analyse operational parameters such as dosing factor, first layer thickness, and recoater velocity.

Case	Dosing factor (D_F)	First layer thickness (LT_F, μm)	Recoater velocity (V_R, mm s^{-1})
1	1.0	50	50
2	1.5	50	50
3	2.0	50	50
4	1.0	100	50
5	1.0	150	50
6	1.0	50	100
7	1.0	50	150

Table 6

Comparison of D_{10}, D_{50}, and D_{90} values of PSD data from simulations with varying dosing factor.

Case	Zone	D_{10}	D_{50}	D_{90}
$D_F = 1.0$ (Bulk volume)	Zone B	22.11	35.49	51.67
	Zone E	23.81	38.41	54.75
$D_F = 1.5$ (Bulk volume)	Zone B	21.48	34.59	50.40
	Zone E	23.24	36.82	53.97
$D_F = 2.0$ (Bulk volume)	Zone B	21.09	33.84	50.19
	Zone E	22.61	36.56	53.02

that the packing densities in all zones align closely with the experimental findings. As shown in Fig. 5(b), the particle size distribution from the experiments reveals that the small-sized particles are more in zone B and large-sized particles are more in zone E compared to the original powder (powder used for the spreading). The PSD in zones B and E remained invariant along the direction of gas flow, indicating that the gas flow did not exert any significant influence on the variation of PSD. The particle size distribution obtained from simulations in different zones for the whole volume is in good agreement with the experiments, as shown in Fig. 5(c). This characteristic of PSD in zones B and E signifies the segregation of powder according to their size during spreading. The segregation happens when the smaller powder particles percolate through the temporary void regions of a powder pile before recoater and settling down at the beginning of the spreading platform, and the larger particles accumulate at the end of the platform. Hence, zones B and E contain large fractions of smaller-sized particles and large-sized particles, respectively. For the bulk volume, the PSD in different zones is shown in Fig. 5(d). It can also be observed that the PSD in zone C is in good agreement with the original PSD (see Fig. 5(d)), it may be inferred that zone C (centre zone) is the optimal zone to manufacture the components because of the homogeneity of the powder bed (high packing density and low segregation effect). The corresponding D_{10}, D_{50}, and D_{90} values of PSD data obtained from experiments and simulations are presented in Table 4. To investigate the effect of process parameters like dosing factor, first layer thickness and recoater velocity on the homogeneity of the powder bed, several other simulation cases (see Table 5) were analysed.

3.2. Influence of the dosing factor

In this section, the influence of the dosing factor on the homogeneity of the powder layers is discussed. With increasing dosing factor, there will be no wedge formation as seen for ($D_F = 1.0$) in Section 3.1. With the powder present in the dispenser, a maximum of 8 and 11 layers were spread onto the platform with $D_F = 1.5$ and $D_F = 2.0$, respectively (see Movie C2, Movie C3). Fig. 6(a) depicts the well-formed spread layers generated while spreading with $D_F = 2.0$. The variation of packing density and normalised powder loss with spread layers are shown in Figs. 6(b) and 6(c). For the initial few layers (1 to 3 layers), the packing density of the spread layer with a higher dosing factor is

less than that obtained for $D_F = 1.0$, and this is because the increase in D_F leads to a higher mass, thereby creating a higher scraping effect on powders [54]. With an increase in the number of layers, the packing density of the spread layer with a higher dosing factor is higher than that obtained for $D_F = 1.0$. With further increase in the layers, the packing density of the spread layers stabilises, as shown in Fig. 6(b). It can be observed that the packing density in the bulk volume is the same for any dosing factor. This is expected as the bulk volume of all cases is the same, and this is the significance of investigating the bulk volume. For the dosing factor of one, with an increasing number of spread layers, the powder loss decreases and attains zero after the fourth layer. For higher dosing factors, the powder loss decreases for the first five layers and then increases. This phenomenon correlates with the packing density of the spread layer, as the minima of the powder loss curves coincide with the bulk volume packing density, reaching at a steady state value of approximately 55%. The normalised powder loss is estimated as follows:

Normalised powder loss

$$= D_F \frac{\text{Mass of the powder at the exit}}{\text{Mass of the powder input from dispenser or dosage}} \qquad (3.2)$$

Wischeropp et al. [64] determined that the gap between solidified surface and recoater (actual layer height) increases for the initial layers due to powder loss (attributed to phenomena such as powder spatter and denudation effect) and solidified part formation. This height stabilises at a steady state after approximately seven layers. The higher gap in the initial layers requires a high powder dosage, resulting in minimal powder loss. Once the steady state is reached, the dosage will be lowered to reduce the powder loss. Therefore, in reality, powder loss for the initial layers (5 layers in simulations) may not be as high, as shown in Fig. 6(c).

The eight spread layers of the spreading process with $D_F = 1.0$, $D_F = 1.5$ and $D_F = 2.0$, respectively, are shown in Fig. 7(a). The packing density in the zone B and E is approximately 57.5% with variation of the dosing factor. The PSD in different zones for the $D_F = 1.0$, $D_F = 1.5$ and $D_F = 2.0$ are shown in Figs. 7(b) to 7(d). Additionally the corresponding D_{10}, D_{50}, and D_{90} values of PSD data obtained from simulations with different dosing factors are listed in Table 6. As the dosing factor increases, the large fraction of large-sized particles in zone E decreases, aligning more closely with the particle size distribution (PSD) of the original powder. In contrast, the PSD of zone B is shifted towards the left, implying a large fraction of smaller particles at the beginning of the spreading platform. The results show that the increase in the dosing factor reduces the segregation effects at the end zone of the platform. However, there exists a large number of smaller particles in zone B (see the green curve in Figs. 7(c) and 7(d)).

3.3. Effect of the first layer thickness

In experiments, there is flexibility in varying the first layer thickness manually. After the first layer, the spreading platform of the setup lowers only by the layer thickness, i.e., 50 μm. In this simulation, the thickness of the first layer was increased by 100 μm and 150 μm as shown in Table 5 (see Movie C4, Movie C5). The visualisation of a few spread

(a)

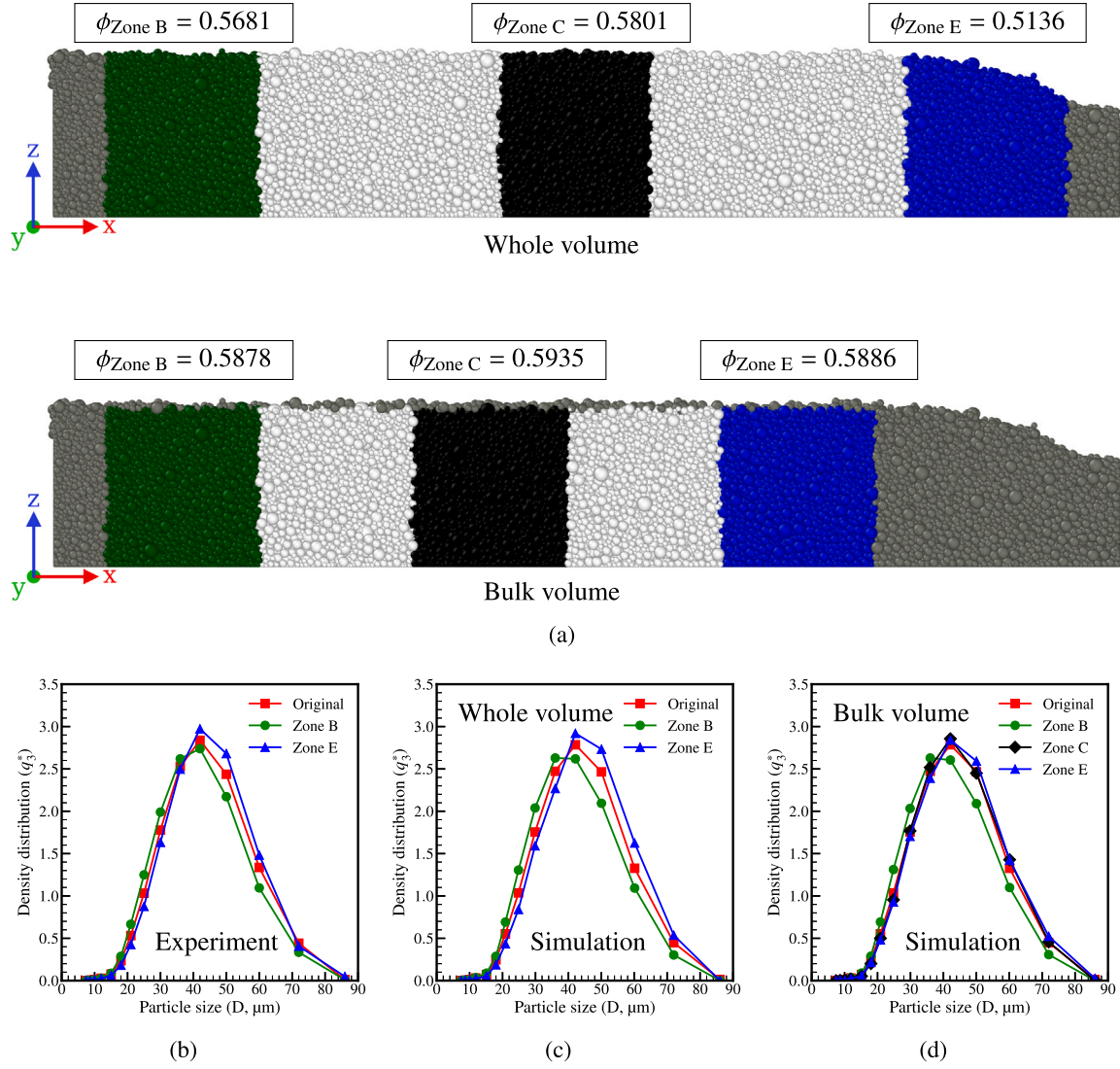(b)   (c)   (d)

Fig. 5. (a) Visualisation of sixteen spread layers for whole and bulk volume indicating packing density in different zones. Comparison of particle size distribution in different zones with original powder: (b) experimental data, (c) whole volume from simulation, and (d) bulk volume from simulation.

layers for the case of spreading with $LT_F = 150\,\mu m$ is shown in Fig. 8(a). As seen in Section 3.1, there is also a wedge formation in this case due to the scarcity of the powder at the end of the platform. Fig. 8(b) depicts the variation of packing density with the spread layers for different first-layer thicknesses. For the initial few layers (1 to 6 layers), the packing density of the spread layers with a higher first layer thickness is higher than for a first layer 50 μm thick ($LT_F = 50\,\mu m$). With the increase in the layers, the packing density of the spread layers stabilises, and this phenomenon can be clearly observed in the bulk volume. Increasing the first layer thickness is also beneficial in decreasing the powder loss, as shown in Fig. 8(c). Therefore, increasing the first layer thickness increases the packing density and reduces powder loss. However, as the powder layer thickens, binding the solidified layer to the platform becomes more challenging. To prevent this condition, it is recommended not to excessively increase layer thickness. Previous research [65–67] indicated that the melt pool depth typically ranges from 100 μm to 200 μm, highlighting the importance of maintaining optimal layer thickness for effective binding and part quality in LPBF. This study suggests increasing only the first layer thickness, and it is not

recommended to increase the subsequent layer thickness as it adversely affects the quality of the parts [53,68].

The sixteen spread layers of the spreading process with $LT_F = 100\,\mu m$ and $LT_F = 150\,\mu m$ are shown in Fig. 9(a). The packing density at zones B and E are the same for both cases, approximately 0.59. The PSD of the zones for the case of $LT_F = 100\,\mu m$ and $LT_F = 150\,\mu m$ are shown in Figs. 9(b) and 9(c), respectively. Additionally the corresponding D_{10}, D_{50}, and D_{90} values of PSD data obtained from simulations with varying first layer thickness are listed in Table 7. The phenomenon of having a large number of smaller-sized particles in zone B does not change with the increase in first-layer thickness. The number of large particles in zone E increases with an increase in the thickness of the first layer.

3.4. Influence of the recoater velocity

In this section, the influence of the recoater velocity on the homogeneity of the powder bed is discussed. As mentioned in Section 1, the recoater velocity (V_R) is one of the critical process parameters in LPBF.
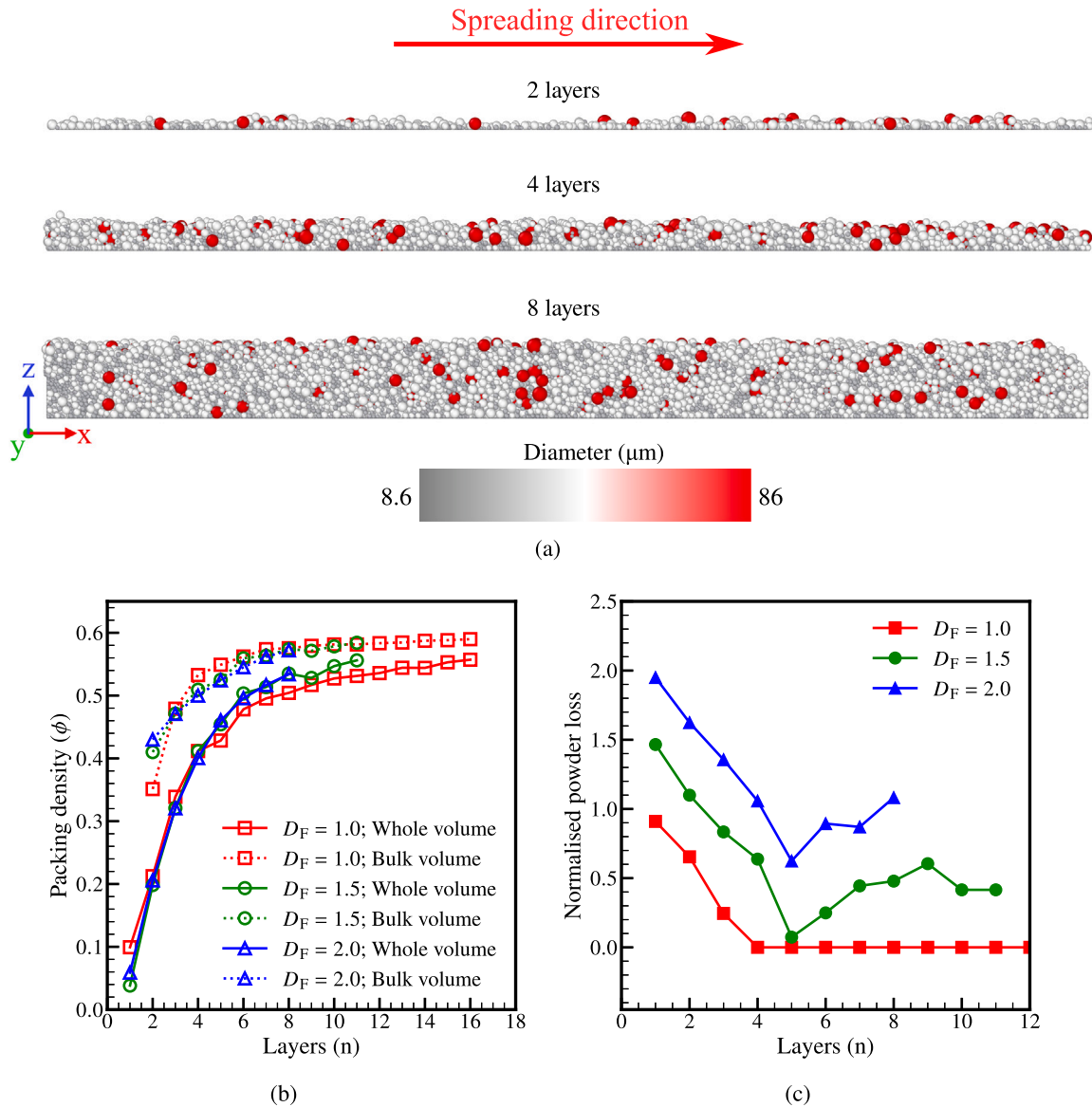
Fig. 6. (a) Visualisation of the spread layer generated with $D_F = 2.0$. Variation of (b) packing density in whole and bulk volumes, and (c) powder loss as a function of the number of spread layers for different dosing factors.

Table 7
Comparison of D_{10}, D_{50}, and D_{90} values of PSD data from simulations with varying first layer thickness.

Case	Zone	D_{10}	D_{50}	D_{90}
$LT_F = 100\,\mu m$	Zone B	21.85	34.65	50.96
(Bulk volume)	Zone E	23.39	37.60	55.56
$LT_F = 150\,\mu m$	Zone B	22.03	34.71	51.16
(Bulk volume)	Zone E	23.68	37.93	55.77

Optimising the recoater velocity is important as it not only minimises spreading time but also contributes to a substantial reduction in overall production time. The multi-layer spreading simulations were carried out with higher recoater velocities such as 100 and 150 mm s^{-1} (see Movie C6, Movie C7) and compared with the case of $V_R = 50$ mm s^{-1} discussed in Section 3.1. With the higher recoater velocity, the initial few layers are formed with high porosity and are thinner, compared with what is obtained with a lower recoater velocity (compare the fourth layer in Figs. 4(a) and 10(a)). As the spreading process advances,

the surface of the powder bed generated is extremely rough (see the layers 8, 12, 16 in Figs. 4(a) and 10(a)). Due to high porosity and surface roughness, the powder is available till the end of the platform, and therefore with increasing recoater velocity, there will be no wedge formation, unlike for the case of 50 mm s^{-1} (see Section 3.1). The variation of packing density and normalised powder loss with spread layers for different recoater velocities are shown in Figs. 10(b) and 10(c). For the initial few layers, the packing density of the powder bed decreases with the increase in recoater velocity. Continuing the spreading process, the packing density in both the whole (WV) and bulk (BV) volumes stabilises at a lower value of approximately 52% compared to the case with a recoater velocity of 50 mm s^{-1}, which achieves a packing density of 56%, as shown in Fig. 10(b). A decrease in the packing density with an increase in the spreading velocity is investigated for the single layer in past studies via experiments and simulations [15,53,69,70]. The powder loss for the case with $V_R = 100$ mm s^{-1} is similar to the case for $V_R = 50$ mm s^{-1}, whereas for the case with $V_R = 150$ mm s^{-1} the powder loss is non-zero for the layers above 6, as shown in Fig. 10(c).

The sixteen spread layers with $V_R = 100$ mm s^{-1} and $V_R = 150$ mm s^{-1} are shown in Fig. 11(a). It can be noticed an increase in the surface
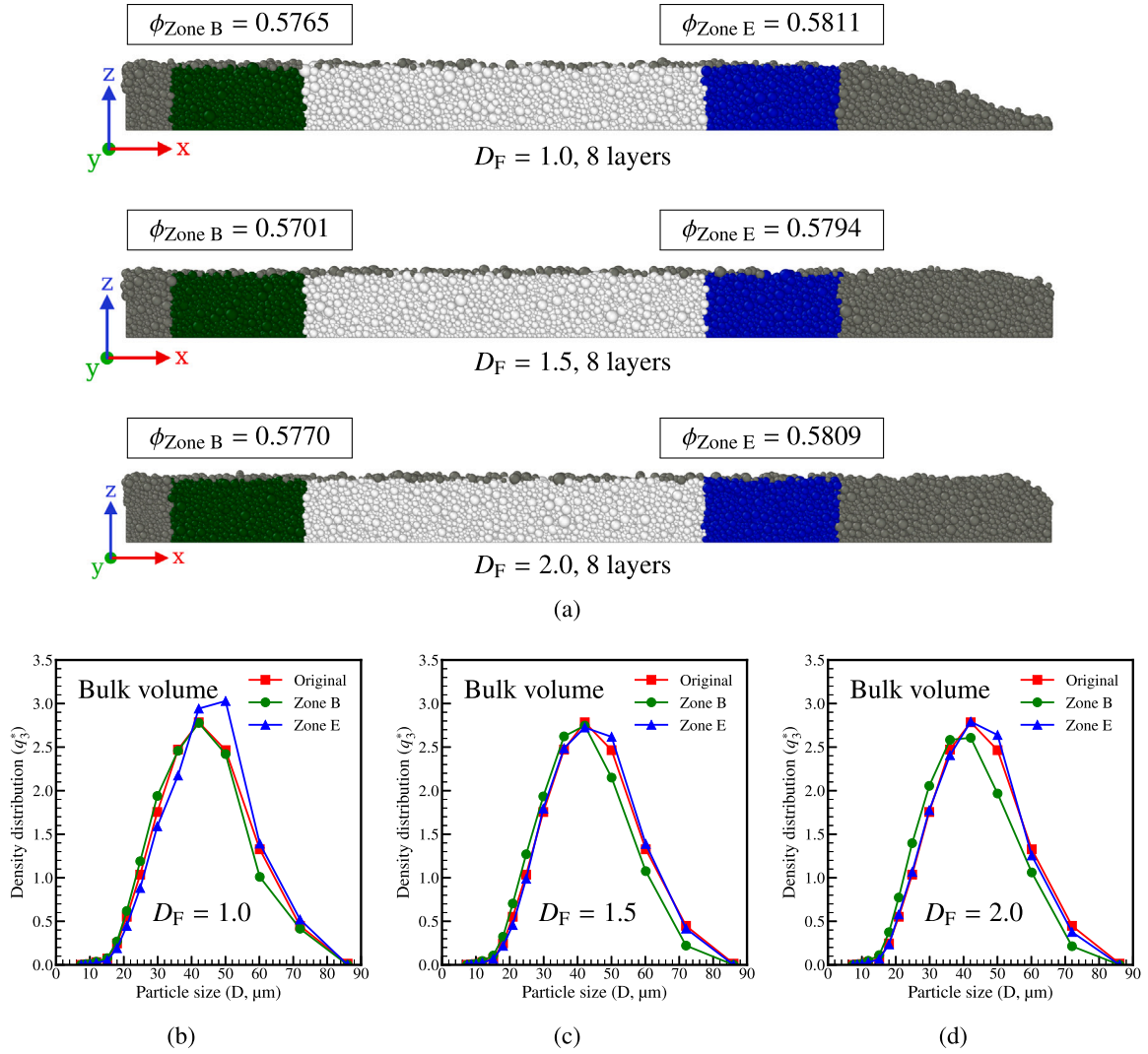
Fig. 7. (a) Visualisation of the eight spread layers of the case with $D_F = 1.0$, $D_F = 1.5$, and $D_F = 2.0$, respectively, indicating packing density in different zones of bulk volume. Comparison of particle size distribution in zones B and E with original powder of the case with (b) $D_F = 1.0$, (c) $D_F = 1.5$, and (d) $D_F = 2.0$.

roughness of the powder bed with an increase in the recoater velocity (compare Figs. 5(a) and 11(a)). Due to the higher surface roughness of the powder bed, packing density at zone E is smaller than that of zone B for both cases, as shown in Fig. 11(a). Chen et al. [44] investigated the influence of recoater velocity on the powder bed quality. The authors reported that even though higher velocity ($240\,\mathrm{mm\,s^{-1}}$) reduces the packing density of the powder bed, it unexpectedly improves the quality of manufactured parts (with lower porosity). Additionally, it stated that for the first few layers, high recoater velocity is unfavourable. However, once the powder layers reach a steady state, parts can be manufactured with higher velocities and better mechanical properties. Furthermore, the authors highlighted that a major disadvantage of high recoater velocity is the reduced dimensional accuracy of the final product. In the current work, it is observed that with an increase in the recoater velocity, the smaller-sized particles do not percolate, leading to lower segregation effects. Hence, PSD in zones B and E for the case with the $V_R = 100\,\mathrm{mm\,s^{-1}}$ and $V_R = 150\,\mathrm{mm\,s^{-1}}$ are exactly similar to that of original powder indicating the lower segregation effect, as shown in Figs. 11(b) and 11(c) (see Table 8 for corresponding D_{10}, D_{50}, and D_{90} values of PSD data obtained for different recoater velocities). The lower segregation effect might improve the quality of the manufactured product.

Table 8
Comparison of D_{10}, D_{50}, and D_{90} values of PSD data from simulations with varying recoater velocity.

Case	Zone	D_{10}	D_{50}	D_{90}
$V_R = 100\,\mathrm{mm\,s^{-1}}$	Zone B	22.72	36.34	53.57
(Bulk volume)	Zone E	22.70	37.16	53.80
$V_R = 150\,\mathrm{mm\,s^{-1}}$	Zone B	22.96	36.85	54.39
(Bulk volume)	Zone E	22.88	37.05	54.14

4. Conclusions

In the present study, experiments and DEM simulations were carried out to analyse the homogeneity of the powder bed in LPBF. The computational framework was developed, integrating the cohesion number scaling and dynamic domain technique with GPU computing to facilitate rapid particle-scale simulations for the computationally expensive powder spreading process. The quality of the powder bed was investigated through multiple layers of spreading simulations along with the dispenser. The influence of the process parameters such as dosing factor, first layer thickness and recoater velocity on the homogeneity of the powder bed was analysed, and the key findings are
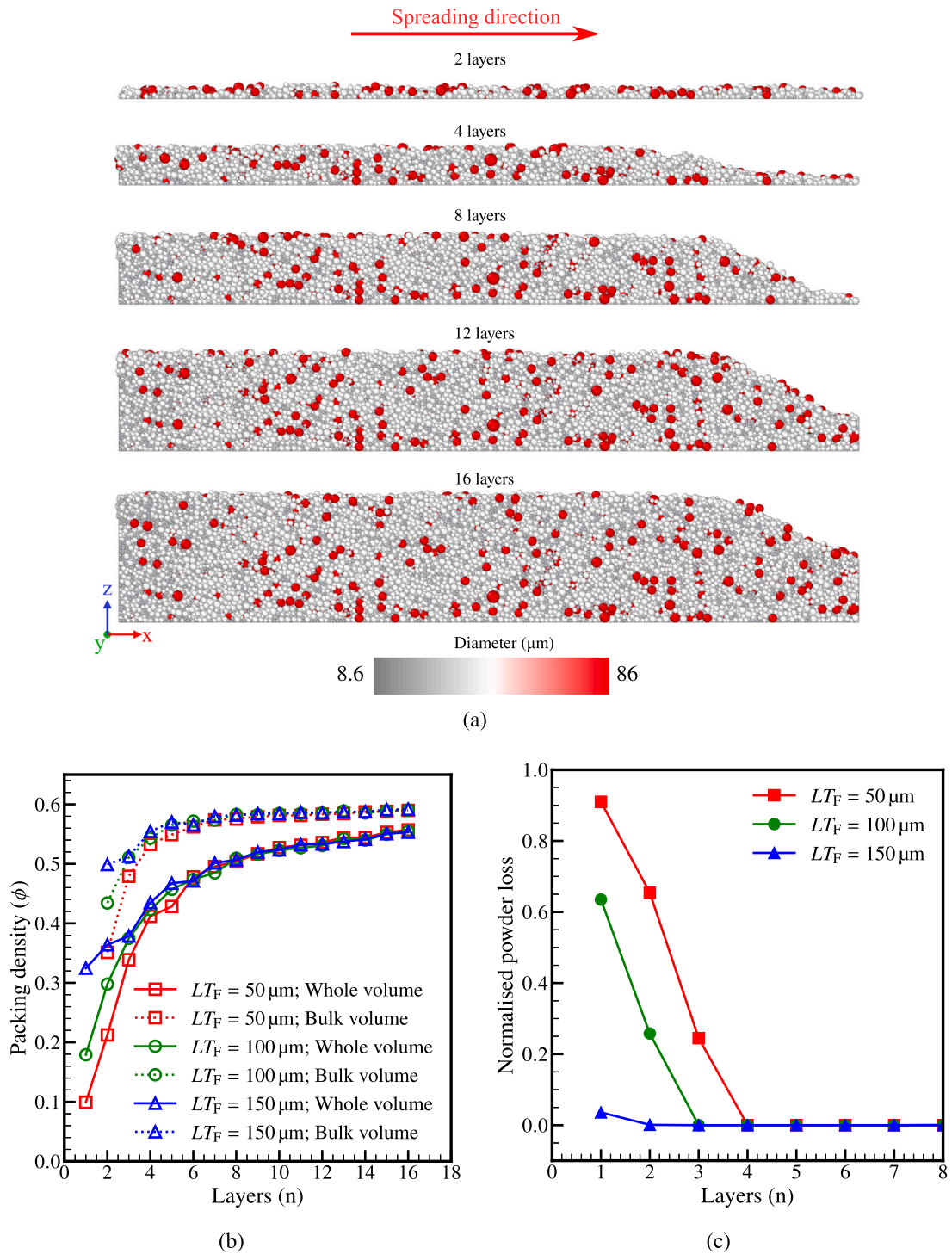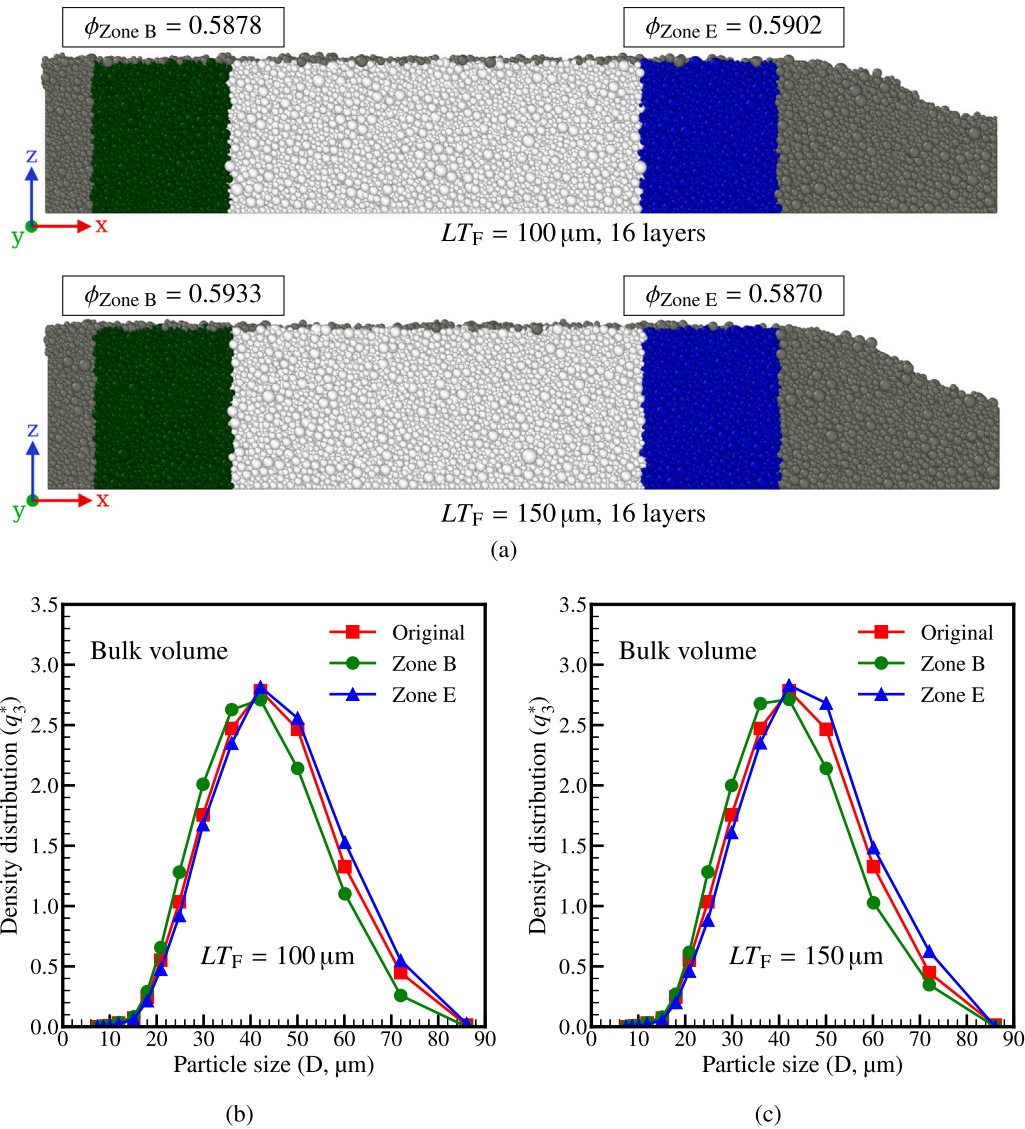
Fig. 8. (a) Visualisation of the spread layer generated with $LT_F = 150\,\mu m$, (b) variation of packing density in whole and bulk volumes for different first layer thicknesses, and (c) powder loss with the number of spread layers with an increase in the first layer thickness.

summarised as follows:

- With a dosing factor of one, the packing density of the spread layers increases with the number of layers. It stabilises to a value of approximately 56%, which is in good agreement with experimental findings. The packing densities in different zones (beginning, centre and end) of the sixteenth layer are the same, with a value of approximately 59%.

- Additionally, the PSD in extreme zones of the 16-layer bed are also in good agreement with experimental findings. It was observed that the large number of small-sized particles in zone B (beginning of the platform) and the large number of large-sized particles in zone E (end of the platform) signify the segregation of powder particles due to the percolation effect. The PSD in the centre zone is similar to that of the original powder, suggesting

$\phi_{\text{Zone B}} = 0.5878$ $\phi_{\text{Zone E}} = 0.5902$

$LT_{\text{F}} = 100\,\mu\text{m}$, 16 layers

$\phi_{\text{Zone B}} = 0.5933$ $\phi_{\text{Zone E}} = 0.5870$

$LT_{\text{F}} = 150\,\mu\text{m}$, 16 layers

(a)

(b)

(c)

Fig. 9. (a) Visualisation of sixteen spread layers of the case with $LT_{\text{F}} = 100\,\mu\text{m}$ and $LT_{\text{F}} = 150\,\mu\text{m}$ indicating packing density in different zones. Comparison of particle size distribution in zones B and E with original powder for the case (b) $LT_{\text{F}} = 100\,\mu\text{m}$, and (c) $LT_{\text{F}} = 150\,\mu\text{m}$.

it is the optimal zone for component manufacturing due to its higher packing density and lower segregation effects, resulting in a homogeneous zone.

- By increasing the dosing factor, the packing density is slightly higher, and stabilisation of the packing density takes place for a lesser number of layers. The powder loss is higher with a higher dosing factor. Increasing the dosing factor minimises but does not completely eliminate segregation effects.
- Increasing the first layer thickness (with the dosing factor of one) minimises powder loss and results in higher packing density. However, an increase in the first layer thickness increases the segregation effects.
- Increasing recoater velocity (with the dosing factor of one) decreases the packing density and the surface quality of the powder bed. In contrast to the dosing factor and first layer thickness, an increase in the recoater velocity decreases the segregation effects.

This study makes several significant contributions to the field of additive manufacturing. By providing a comprehensive analysis of powder bed quality through multi-layer powder spreading, it bridges the gap between single-layer and multi-layer studies. The integration of experimental measurements and numerical simulations offers a robust characterisation of the powder bed, encompassing both micro-scale particle interactions and macro-scale properties like packing density and surface roughness of the bed. The findings of this research have important implications for optimising LPBF processes and enhancing the performance of additive manufacturing parts.

Although this study presents a practical approach (quantitative analysis) to estimating powder bed homogeneity (using packing density, powder loss, and PSD qualitative), detailed investigations of powder dynamics (force, contact network and velocity analyses of the particles) leading to the percolation effect would provide greater clarity on techniques to minimise powder segregation. Furthermore, the implementation of the melting and solidification models with powder spreading on a large scale and with appropriate contact models (cohesive model as presented in this work) will give more insight into the process, powder consumption, and operational conditions.
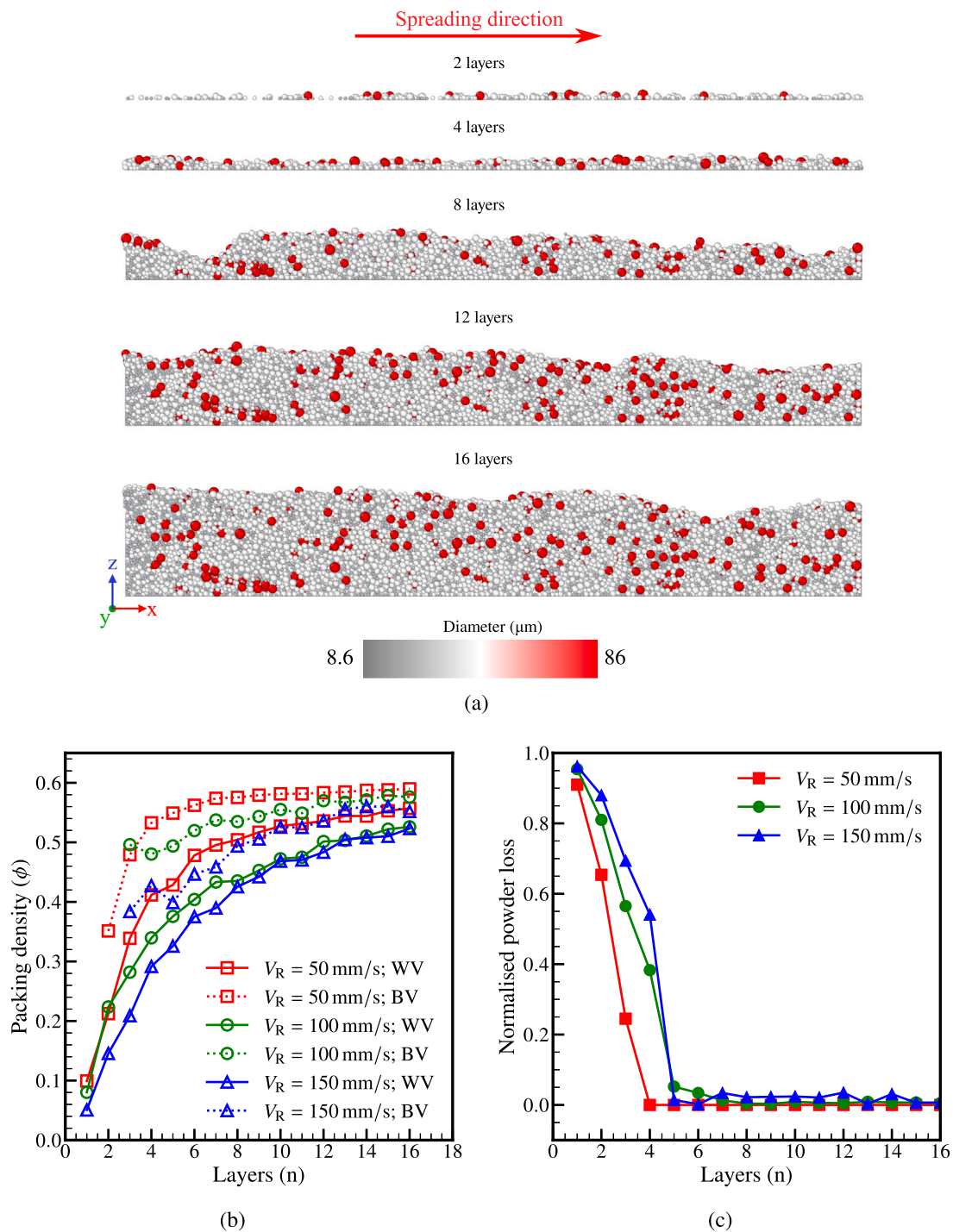
Fig. 10. (a) Visualisation of the spread layer generated with $V_R = 150\,\mathrm{mm\,s^{-1}}$, (b) variation of packing density in whole (WV) and bulk volumes (BV) for different recoater velocities, and (c) powder loss with the number of spread layers with an increase in the recoater velocity.

CRediT authorship contribution statement

Sujith Reddy Jaggannagari: Writing – original draft, Visualization, Methodology, Investigation, Formal analysis, Conceptualization. **Wen Hao Kan:** Writing – review & editing, Investigation. **Louis N.S. Chiu:** Supervision, Conceptualization. **Gwénaëlle Proust:** Writing – review & editing, Supervision. **Aijun Huang:** Supervision. **Yixiang Gan:** Writing – review & editing, Supervision, Conceptualization. **Ratna Kumar Annabattula:** Writing – review & editing, Supervision, Resources, Conceptualization.

Declaration of competing interest

The authors declare that they have no known competing financial interests or personal relationships that could have appeared to influence the work reported in this paper.
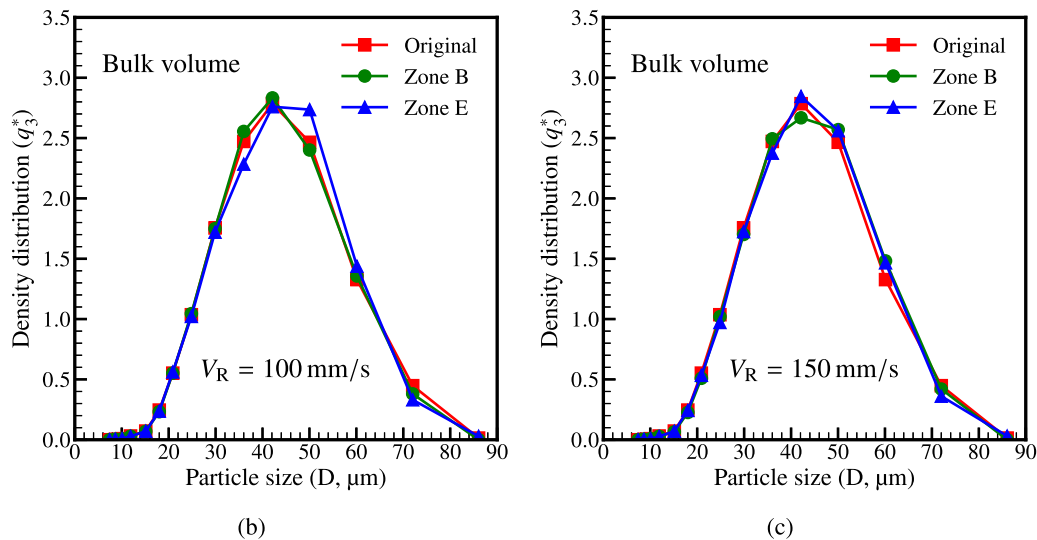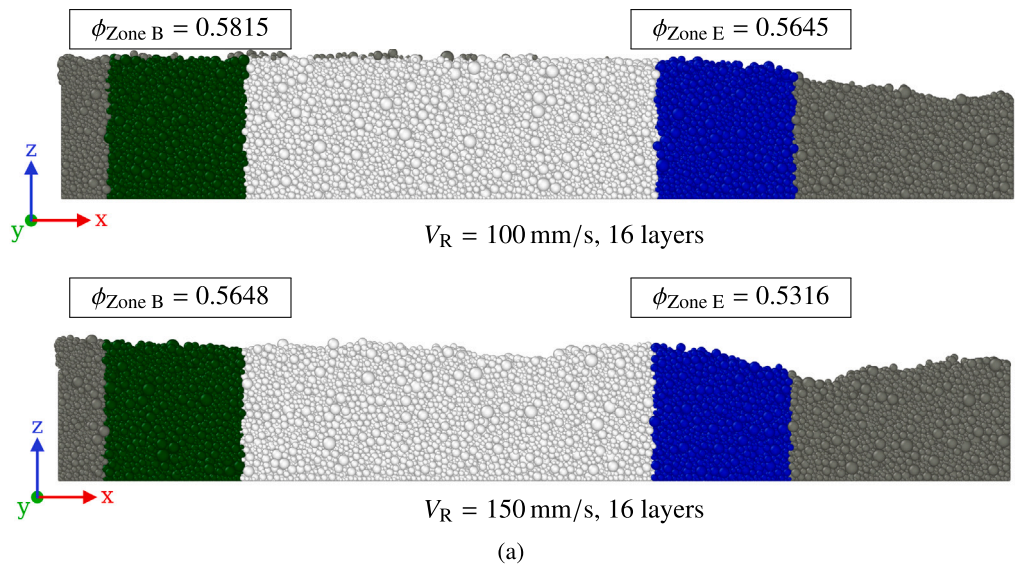
Fig. 11. (a) Visualisation of sixteen spread layers of the case with $V_R = 100\,\mathrm{mm\,s^{-1}}$ and $V_R = 150\,\mathrm{mm\,s^{-1}}$ indicating packing density in different zones. Comparison of particle size distribution in zones B and E with original powder for the case (b) $V_R = 100\,\mathrm{mm\,s^{-1}}$, and (c) $V_R = 150\,\mathrm{mm\,s^{-1}}$.

Appendix A. Supplementary data

Supplementary material related to this article can be found online at https://doi.org/10.1016/j.addma.2024.104571.

Data availability

Data will be made available on request.

References

[1] D. Gu, X. Shi, R. Poprawe, D.L. Bourell, R. Setchi, J. Zhu, Material-structure-performance integrated laser-metal additive manufacturing, Science 372 (6545) (2021) eabg1487.

[2] I. Campbell, D. Bourell, I. Gibson, Additive manufacturing: rapid prototyping comes of age, Rapid Prototyp. J. 18 (4) (2012) 255–258.

[3] J. Xu, T. Ma, R.L. Peng, S. Hosseini, Effect of post-processes on the microstructure and mechanical properties of laser powder bed fused IN718 superalloy, Addit. Manuf. 48 (2021) 102416.

[4] Y. Wu, M. Li, J. Wang, Y. Wang, X. An, H. Fu, H. Zhang, X. Yang, Q. Zou, Powder-bed-fusion additive manufacturing of molybdenum: Process simulation, optimization, and property prediction, Addit. Manuf. 58 (2022) 103069.

[5] M.Y. Shaheen, A.R. Thornton, S. Luding, T. Weinhart, The influence of material and process parameters on powder spreading in additive manufacturing, Powder Technol. 383 (2021) 564–583.

[6] D. Oropeza, R.W. Penny, D. Gilbert, A.J. Hart, Mechanized spreading of ceramic powder layers for additive manufacturing characterized by transmission X-ray imaging: Influence of powder feedstock and spreading parameters on powder layer density, Powder Technol. 398 (2022) 117053.

[7] J.P. Oliveira, A. LaLonde, J. Ma, Processing parameters in laser powder bed fusion metal additive manufacturing, Mater. Des. 193 (2020) 108762.

[8] S. Mojumder, Z. Gan, Y. Li, A. Al Amin, W.K. Liu, Linking process parameters with lack-of-fusion porosity for laser powder bed fusion metal additive manufacturing, Addit. Manuf. 68 (2023) 103500.

[9] Y. He, A. Hassanpour, A.E. Bayly, Linking particle properties to layer characteristics: Discrete element modelling of cohesive fine powder spreading in additive manufacturing, Addit. Manuf. 36 (2020) 101685.

[10] H. Chen, Q. Wei, Y. Zhang, F. Chen, Y. Shi, W. Yan, Powder-spreading mechanisms in powder-bed-based additive manufacturing: Experiments and computational modeling, Acta Mater. 179 (2019) 158–171.

[11] K. Riener, N. Albrecht, S. Ziegelmeier, R. Ramakrishnan, L. Haferkamp, A.B. Spierings, G.J. Leichtfried, Influence of particle size distribution and morphology on the properties of the powder feedstock as well as of AlSi10Mg parts produced by laser powder bed fusion (LPBF), Addit. Manuf. 34 (2020) 101286.

[12] J.H. Tan, W.L.E. Wong, K.W. Dalgarno, An overview of powder granulometry on feedstock and part performance in the selective laser melting process, Addit. Manuf. 18 (2017) 228–255.

[13] S. Vock, B. Klöden, A. Kirchner, T. Weißgärber, B. Kieback, Powders for powder bed fusion: a review, Progr. Addit. Manuf. 4 (2019) 383–397.

[14] S. Yim, H. Bian, K. Aoyagi, K. Yamanaka, A. Chiba, Spreading behavior of Ti48Al2Cr2Nb powders in powder bed fusion additive manufacturing process: Experimental and discrete element method study, Addit. Manuf. 49 (2022) 102489.

[15] H. Chen, Y. Chen, Y. Liu, Q. Wei, Y. Shi, W. Yan, Packing quality of powder layer during counter-rolling-type powder spreading process in additive manufacturing, Int. J. Mach. Tools Manuf. 153 (2020) 103553.

[16] L. Cordova, T. Bor, M. de Smit, M. Campos, T. Tinga, Measuring the spreadability of pre-treated and moisturized powders for laser powder bed fusion, Addit. Manuf. 32 (2020) 101082.

[17] S. Yim, J. Sun, K. Minowa, H. Wang, K. Aoyagi, K. Yamanaka, A. Chiba, In-situ observation of powder spreading in powder bed fusion metal additive manufacturing process using particle image velocimetry, Addit. Manuf. 78 (2023) 103823.

[18] M. Stephan, G. Roux, A. Burr, C. Ablitzer, J.-P. Garandet, Identification of the influential DEM contact law parameters on powder bed quality and flow in additive manufacturing configurations, Powder Technol. 429 (2023) 118937.

[19] R. Xu, W. Nan, Analysis of the metrics and mechanism of powder spreadability in powder-based additive manufacturing, Addit. Manuf. 71 (2023) 103596.

[20] Y. He, A. Hassanpour, A.E. Bayly, Combined effect of particle size and surface cohesiveness on powder spreadability for additive manufacturing, Powder Technol. 392 (2021) 191–203.

[21] D.S. Nasato, H. Briesen, T. Pöschel, Influence of vibrating recoating mechanism for the deposition of powders in additive manufacturing: Discrete element simulations of polyamide 12, Addit. Manuf. 48 (2021) 102248.

[22] W. Nan, Y. Gu, Experimental investigation on the spreadability of cohesive and frictional powder, Adv. Powder Technol. 33 (3) (2022) 103466.

[23] L. Wang, A. Yu, E. Li, H. Shen, Z. Zhou, Effects of spreader geometry on powder spreading process in powder bed additive manufacturing, Powder Technol. 384 (2021) 211–222.

[24] A. Mussatto, R. Groarke, A. O'Neill, M.A. Obeidi, Y. Delaure, D. Brabazon, Influences of powder morphology and spreading parameters on the powder bed topography uniformity in powder bed fusion metal additive manufacturing, Addit. Manuf. 38 (2021) 101807.

[25] A. Mussatto, R. Groarke, A. Ahmed, I.U. Ahad, R.K. Vijayaraghavan, A. O'Neill, P. McNally, Y. Delaure, D. Brabazon, et al., Evaluation via powder metallurgy of nano-reinforced iron powders developed for selective laser melting applications, Mater. Des. 182 (2019) 108046.

[26] S.E. Brika, M. Letenneur, C.A. Dion, V. Brailovski, Influence of particle morphology and size distribution on the powder flowability and laser powder bed fusion manufacturability of ti-6al-4v alloy, Addit. Manuf. 31 (2020) 100929.

[27] C. Pleass, S. Jothi, Influence of powder characteristics and additive manufacturing process parameters on the microstructure and mechanical behaviour of inconel 625 fabricated by selective laser melting, Addit. Manuf. 24 (2018) 419–431.

[28] A. Phua, C. Doblin, P. Owen, C.H. Davies, G.W. Delaney, The effect of recoater geometry and speed on granular convection and size segregation in powder bed fusion, Powder Technol. 394 (2021) 632–644.

[29] M. Daňa, I. Zetková, P. Hanzl, The influence of a ceramic recoater blade on 3D printing using direct metal laser sintering, Manuf. Technol. 19 (1) (2019) 23–28.

[30] A.K. Tigga, S.A. Kumar, N.B. Kenchappa, A. Pathania, Effects of graded powder dosage factors on the densification of LPBF processed Inconel 718, Trans. Indian Inst. Met. 76 (12) (2023) 3473–3481.

[31] F. Ahmed, U. Ali, D. Sarker, E. Marzbanrad, K. Choi, Y. Mahmoodkhani, E. Toyserkani, Study of powder recycling and its effect on printed parts during laser powder-bed fusion of 17-4 PH stainless steel, J. Mater. Process. Technol. 278 (2020) 116522.

[32] M. Ahmed, M. Pasha, W. Nan, M. Ghadiri, A simple method for assessing powder spreadability for additive manufacturing, Powder Technol. 367 (2020) 671–679.

[33] Z. Chen, X. Wu, D. Tomus, C.H. Davies, Surface roughness of selective laser melted Ti-6Al-4V alloy components, Addit. Manuf. 21 (2018) 91–103.

[34] P.A. Cundall, O.D. Strack, A discrete numerical model for granular assemblies, Geotechnique 29 (1979) 47–65.

[35] H. Chen, Q. Wei, S. Wen, Z. Li, Y. Shi, Flow behavior of powder particles in layering process of selective laser melting: Numerical modeling and experimental verification based on discrete element method, Int. J. Mach. Tools Manuf. 123 (2017) 146–159.

[36] D. Yao, J. Wang, M. Li, T. Zhao, Y. Cai, X. An, R. Zou, H. Zhang, H. Fu, X. Yang, et al., Segregation of 316L stainless steel powder during spreading in selective laser melting based additive manufacturing, Powder Technol. 397 (2022) 117096.

[37] H. Mindt, M. Megahed, N. Lavery, M. Holmes, S. Brown, Powder bed layer characteristics: the overseen first-order process input, Metall. Mater. Trans. A 47 (2016) 3811–3822.

[38] W. Nan, M. Pasha, T. Bonakdar, A. Lopez, U. Zafar, S. Nadimi, M. Ghadiri, Jamming during particle spreading in additive manufacturing, Powder Technol. 338 (2018) 253–262.

[39] S. Shamsdini, M. Ghoncheh, M. Mohammadi, Effect of recoater-blade type on the mechanical properties and microstructure of additively manufactured maraging steels, Mater. Sci. Eng. A 812 (2021) 141104.

[40] Z. Snow, R. Martukanitz, S. Joshi, On the development of powder spreadability metrics and feedstock requirements for powder bed fusion additive manufacturing, Addit. Manuf. 28 (2019) 78–86.

[41] M. Horn, M. Schmitt, L. Langer, G. Schlick, C. Seidel, Laser powder bed fusion recoater selection guide—Comparison of resulting powder bed properties and part quality, Powder Technol. 434 (2024) 119356.

[42] T.-P. Le, X. Wang, K.P. Davidson, J.E. Fronda, M. Seita, Experimental analysis of powder layer quality as a function of feedstock and recoating strategies, Addit. Manuf. 39 (2021) 101890.

[43] L. Wang, Z. Zhou, E. Li, H. Shen, A. Yu, Powder deposition mechanism during powder spreading with different spreader geometries in powder bed fusion additive manufacturing, Powder Technol. 395 (2022) 802–810.

[44] H. Chen, T. Cheng, Z. Li, Q. Wei, W. Yan, Is high-speed powder spreading really unfavourable for the part quality of laser powder bed fusion additive manufacturing? Acta Mater. 231 (2022) 117901.

[45] L. Scime, J. Beuth, Anomaly detection and classification in a laser powder bed additive manufacturing process using a trained computer vision algorithm, Addit. Manuf. 19 (2018) 114–126.

[46] L. Scime, J. Beuth, A multi-scale convolutional neural network for autonomous anomaly detection and classification in a laser powder bed fusion additive manufacturing process, Addit. Manuf. 24 (2018) 273–286.

[47] Y. Lee, S. Simunovic, A.K. Gurnon, Quantification of powder spreading process for metal additive manufacturing, Technical Report, Oak Ridge National Laboratory (ORNL), Oak Ridge, TN (United States), 2019.

[48] R.W. Penny, P.M. Praegla, M. Ochsenius, D. Oropeza, R. Weissbach, C. Meier, W.A. Wall, A.J. Hart, Spatial mapping of powder layer density for metal additive manufacturing via transmission X-ray imaging, Addit. Manuf. 46 (2021) 102197.

[49] J. Wang, D. Yao, M. Li, X. An, S. Li, W. Hou, X. Zhang, G. Yang, J. Wang, L. Wang, Hierarchical effects of multi-layer powder spreading in the electron beam powder bed fusion additive manufacturing of pure tungsten material, Addit. Manuf. 55 (2022) 102835.

[50] L. Cao, W. Guan, Simulation and analysis of LPBF multi-layer single-track forming process under different particle size distributions, Int. J. Adv. Manuf. Technol. 114 (2021) 2141–2157.

[51] Z. Xiang, M. Zhang, R. Yan, Q. Yin, K. Zhang, Powder-spreading dynamics and packing quality improvement for laser powder bed fusion additive manufacturing, Powder Technol. 389 (2021) 278–291.

[52] L. Si, T. Zhang, M. Zhou, M. Li, Y. Zhang, H. Zhou, Numerical simulation of the flow behavior and powder spreading mechanism in powder bed-based additive manufacturing, Powder Technol. 394 (2021) 1004–1016.

[53] D. Yao, X. An, H. Fu, H. Zhang, X. Yang, Q. Zou, K. Dong, Dynamic investigation on the powder spreading during selective laser melting additive manufacturing, Addit. Manuf. 37 (2021) 101707.

[54] S. Wu, Z. Lei, M. Jiang, J. Liang, B. Li, Y. Chen, Experimental investigation and discrete element modeling for particle-scale powder spreading dynamics in powder-bed-fusion-based additive manufacturing, Powder Technol. 403 (2022) 117390.

[55] M.A. Behjani, N. Rahmanian, A. Hassanpour, et al., An investigation on process of seeded granulation in a continuous drum granulator using DEM, Adv. Powder Technol. 28 (10) (2017) 2456–2464.

[56] J. Hærvig, U. Kleinhans, C. Wieland, H. Spliethoff, A.L. Jensen, K. Sørensen, T.J. Condra, On the adhesive JKR contact and rolling models for reduced particle stiffness discrete element simulations, Powder Technol. 319 (2017) 472–482.

[57] Altair EDEM, 2022, URL https://help.altair.com/EDEM/Introducing_EDEM.htm.

[58] W. Nan, M. Ghadiri, Numerical simulation of powder flow during spreading in additive manufacturing, Powder Technol. 342 (2019) 801–807.

[59] M.H. Sehhat, A.T. Sutton, Z. Yates, M.C. Leu, Experimental approach for development of a powder spreading metric in additive manufacturing, Int. J. Adv. Manuf. Technol. 126 (1) (2023) 371–380.

[60] S. Khajepor, O. Ejtehadi, S. Haeri, The effects of interstitial inert gas on the spreading of inconel 718 in powder bed fusion, Addit. Manuf. 75 (2023) 103737.

[61] L.I. Escano, N.D. Parab, L. Xiong, Q. Guo, C. Zhao, K. Fezzaa, W. Everhart, T. Sun, L. Chen, Revealing particle-scale powder spreading dynamics in powder-bed-based additive manufacturing process by high-speed X-ray imaging, Sci. Rep. 8 (1) (2018) 1–11.

[62] S.R. Jaggannagari, R.K. Desu, J. Reimann, Y. Gan, M. Moscardini, R.K. Annabattula, DEM simulations of vibrated sphere packings in slender prismatic containers, Powder Technol. 393 (2021) 31–59.

[63] J. Reimann, A. Abou-Sena, R. Nippen, P. Tafforeau, Pebble bed packing in prismatic containers, Fusion Eng. Des. 88 (9–10) (2013) 2343–2347.

[64] T.M. Wischeropp, C. Emmelmann, M. Brandt, A. Pateras, Measurement of actual powder layer height and packing density in a single layer in selective laser melting, Addit. Manuf. 28 (2019) 176–183.

[65] S. Shrestha, K. Chou, A study of transient and steady-state regions from single-track deposition in laser powder bed fusion, J. Manuf. Process. 61 (2021) 226–235.

[66] M. Khorasani, A. Ghasemi, M. Leary, L. Cordova, E. Sharabian, E. Farabi, I. Gibson, M. Brandt, B. Rolfe, A comprehensive study on meltpool depth in laser-based powder bed fusion of Inconel 718, Int. J. Adv. Manuf. Technol. 120 (3) (2022) 2345–2362.

[67] G. Kaya, F. Yıldız, İ.H. Korkmaz, İ. Kaymaz, A.F. Yetim, T.O. Ergüder, Ç. Şen, Effects of process parameters on selective laser melting of Ti6Al4V-ELI alloy and parameter optimization via response surface method, Mater. Sci. Eng. A 885 (2023) 145581.

[68] R. Wang, D. Garcia, R.R. Kamath, C. Dou, X. Ma, B. Shen, H. Choo, K. Fezzaa, H.Z. Yu, Z. Kong, In situ melt pool measurements for laser powder bed fusion using multi sensing and correlation analysis, Sci. Rep. 12 (1) (2022) 13716.

[69] S. Haeri, Y. Wang, O. Ghita, J. Sun, Discrete element simulation and experimental study of powder spreading process in additive manufacturing, Powder Technol. 306 (2017) 45–54.

[70] E. Li, Z. Zhou, L. Wang, R. Zou, A. Yu, Particle scale modelling of powder recoating and melt pool dynamics in laser powder bed fusion additive manufacturing: a review, Powder Technol. 409 (2022) 117789.